Collinear laser spectroscopy of Ca$^+$: Solving the field-shift puzzle of the $4s\,^2\mathrm{S}_{1/2} \to 4p\,^2\mathrm{P}_{1/2,3/2}$ transitions

Patrick Müller [1,2,*], Kristian König [1,†], Phillip Imgram [1], Jörg Krämer,[1,2] and Wilfried Nörtershäuser [1,2]

[1]*Institut für Kernphysik, Technische Universität Darmstadt, Schlossgartenstrasse 9, 64289 Darmstadt, Germany*
[2]*Helmholtz Forschungsakademie Hessen für FAIR (HFHF), GSI Helmholtzzentrum für Schwerionenforschung, Planckstrasse 1, 64291 Darmstadt, Germany*

High-precision quasisimultaneous collinear/anticollinear laser spectroscopy was used to measure the $4s\,^2\mathrm{S}_{1/2} \to 4p\,^2\mathrm{P}_{1/2}$ (D1) and the $4s\,^2\mathrm{S}_{1/2} \to 4p\,^2\mathrm{P}_{3/2}$ (D2) as well as the three $3d \to 4p$ transitions in the naturally abundant Ca$^+$ isotopes. Thereby, accuracies of approximately 100 kHz were achieved, which enabled an accurate determination of the field-shift ratio in the D2 and D1 lines through a King-plot analysis. Our value of $F_{\mathrm{D2}}/F_{\mathrm{D1}} = 1.0010(23)$ is in excellent agreement with current theoretical predictions, while former experimental results from ion-trap measurements showed a 3σ to 6σ deviation from theory introducing the so-called Ca$^+$ field-shift puzzle. A successful check of consistency was made by combining the measurements of the D1 and D2 lines with those of the $3d \to 4p$ transitions and precise literature values for the $4s \to 3d$ and $3d\,^2\mathrm{D}_{3/2} \to 3d\,^2\mathrm{D}_{5/2}$ transitions. Failing for the previous ion-trap measurements, the check of consistency strongly indicates that our results constitute a solution to this puzzle, supporting the results of atomic theory.

I. INTRODUCTION

Accurate isotope shift and transition frequency measurements are required for a wide variety of applications. In nuclear physics, the information from the isotope shift has been used for almost a century to extract nuclear sizes, namely, changes in the mean-square nuclear charge radius. Especially with the advent of the laser and the installation of laser spectroscopy devices at online facilities, short-lived isotopes became accessible, and still today this is the most accurate technique to determine their charge radii [1]. Isotope shifts are also of interest to study a possible variation in the fine-structure constant in strong gravitational fields of quasars [2,3]. Laser spectroscopic techniques such as resonance ionization mass spectrometry are applied to study extremely rare long-lived radioisotopes, where the isotope shift is actually used to suppress strongly dominant more abundant neighboring isotopes for radiodating of materials or as a tracer for biomedical applications [4]. More recently, it has been proposed to use isotope shift measurements in the search for temporal and spatial variations in the fine-structure constant [5] or in the search for new force mediators [6–9]. In the more classical application at the borderline of atomic and nuclear physics it was also suggested that precise measurements of atomic transitions would offer an alternative path to surface properties of unstable nuclei by determining higher radial moments of nuclei [10]. Such an approach would have to be certified and calibrated on stable isotopes where precise data on these moments are available from elastic electron scattering.

All of these proposals require high experimental accuracy as well as theoretical precision in order to extract the physical observables. To explore the feasibility of the well-established technique of collinear laser spectroscopy for such applications, we investigated five transitions in Ca$^+$ isotopes. We have chosen calcium since former investigations in Ca$^+$ isotopes revealed an unsettling result—the so-called "field-shift puzzle" [11]—that challenged atomic theory and was obtained in high-precision ion-trap measurements. Furthermore, these investigations are a stepping stone towards high-precision measurements of light He-like systems that need to be addressed to facilitate total charge radii determinations for beryllium, boron, and carbon. These measurements will set tighter constraints for *ab initio* nuclear structure theory as well as for QED calculations in light systems whose evaluation is often limited to differences in mean-square nuclear charge radii and the comparably large uncertainties from elastic electron-scattering data [12–14]. To reach the accuracy required for both applications, we had to carefully address several aspects of systematic uncertainties relevant in collinear laser spectroscopy.

Calcium has five stable isotopes ^{40,42,43,44,46}Ca and the extremely long-lived ^{48}Ca, which can be considered stable. Both ^{40}Ca and ^{48}Ca have magic neutron numbers, and their nuclear charge radii are small and almost identical. This is a unique case for all magic isotopes. In the last years, in

---

*pamueller@ikp.tu-darmstadt.de
†Present address: National Superconducting Cyclotron Laboratory, Michigan State University, East Lansing, Michigan 48824, USA.

particular, the investigation of the mean-square nuclear charge radii of the short-lived Ca isotopes towards the neutron and proton drip line via collinear laser spectroscopy has received a lot of attention [15,16]. In both measurements, the charge radius is extracted from the isotope shift, the difference in frequency of an electronic transition between two isotopes. This requires knowledge of the so-called field-shift factor F, which is either extracted from a King plot using known information of nuclear charge radii from muonic atoms or elastic electron scattering [17–19] or derived from atomic theory [20]. Considerable progress has been made in such calculations in recent years, both in *ab initio* calculations based on nonrelativistic quantum electrodynamics in light nuclei [21–23] and in mean-field and coupled-cluster approaches for heavy nuclei [24–26].

Due to the importance of atomic structure calculations for the nuclear charge radius determination, it was concerning that atomic theory was not able to provide consistent results for the ratio of the field shifts in the D1 and D2 transitions of Ca^+ compared with modern high-precision measurements [11]. Even though this ratio should be calculable with much higher precision than its absolute value, none of the state-of-the-art theories was able to reproduce the experimental value obtained using highly sophisticated ion-trap measurements on sympathetically cooled single Ca^+ ions [11,27,28]. Moreover, theory claimed that the experimental value was higher than any theory could account for [11,29]. Even the theoretical value of 1.0051, given by the solution of the Dirac equation for the hydrogenic atom with $Z = 20$, was surpassed. Since the main origin of any correction to this model is the charge screening from the bound electrons, this value constitutes an upper limit. In contrast, previous measurements of Ba^+, the heaviest alkaline-earth metal with stable isotopes, confirmed the theoretical predictions of its field-shift ratio [30,31]. It should also be noted that the isotope shifts of the stable isotopes, reported in Refs. [32] and [11] were used to calibrate the measurements of the short-lived isotopes in Refs. [15] and [16] respectively. Moreover, a comprehensive summary of isotope shifts in transitions of neutral and singly charged calcium was recently published, in which the isotope shifts reported in Refs. [11,28] play a pivotal role since they are used to reevaluate all other published isotope shifts in the corresponding transitions and also influence data in other transitions on the basis of respective King plots and global fittings [33]. The reported accuracy in the trap measurements is considerably higher than that of previously reported collinear measurements, and the trap measurements therefore have a strong weight in the data evaluation.

Here, we report on new measurements of the transition frequencies and isotope shifts in the $4s\,^2S_{1/2} \rightarrow 4p\,^2P_{1/2}$ (D1), the $4s\,^2S_{1/2} \rightarrow 4p\,^2P_{3/2}$ (D2), and the three $3d \rightarrow 4p$ transitions in the naturally most abundant Ca^+ isotopes. In order to reach an accuracy comparable to ion-trap measurements, the Collinear Apparatus for Laser Spectroscopy and Applied Science (COALA) at Technische Universität Darmstadt was specially designed for high-precision applications [34]. Systematic contributions have been investigated in earlier experiments [31,35] and have been resolved in this paper. Doing so, we achieved accurate collinear laser spectroscopy and were able to resolve the Ca^+ field-shift puzzle. Contrary to

the previous measurements, our result is in good agreement with theory. Moreover, it is more consistent with additional high-precision determinations of other transitions, reported recently.

II. METHOD

The isotope shift can be split into the mass shift and the field shift, which originate from the change in the kinetic energy of the center-of-mass motion and the change in the nuclear charge distribution, respectively. The isotope shift of a transition i can thus be written as

$$\delta\nu_i^{A,A'} := \nu_i^{A'} - \nu_i^A = K_i\frac{M_{A'} - M_A}{(M_{A'} + m_e)M_A} + F_i\delta\langle r^2\rangle^{A,A'}, \quad (1)$$

with the mass-shift factor K_i and the field-shift factor F_i. The field shift of a transition i is in lowest order proportional to the change in the mean-square nuclear charge radius $\delta\langle r^2\rangle^{A,A'}$ with proportionality factor $F_i = -Ze^2\Delta|\psi(0)|_i^2/(6h\varepsilon_0)$. Hence it varies with the size of the nucleus and the change in the electron density inside the nucleus $\Delta|\psi(0)|_i^2$ caused by the electronic transition. If isotope shifts in two transitions i and j are determined, the mean-square nuclear charge radius can be eliminated in Eq. (1) to give

$$\mu^{A,A'}\delta\nu_i^{A,A'} = K_i - \frac{F_i}{F_j}K_j + \frac{F_i}{F_j}\mu^{A,A'}\delta\nu_j^{A,A'}, \quad (2)$$

where $\mu^{A,A'} := (M_{A'} + m_e)M_A/(M_{A'} - M_A)$ and $\mu^{A,A'}\delta\nu_i^{A,A'}$ is called the modified isotope shift. Hence the field-shift ratio F_i/F_j can be determined by plotting the modified isotope shifts in transition i against those in j and performing a linear fit [36]. The slope of the line corresponds to the field-shift ratio and can serve as a benchmark for atomic structure calculations.

The electronic ground state of Ca^+ is the $4s\,^2S_{1/2}$ state. Dipole transitions at 397 nm (D1) and 393 nm (D2) lead to the $4p\,^2P_{1/2}$ and $^2P_{3/2}$ levels, respectively. From there, a decay back into the ground state or into one of the metastable $3d\,^2D_{3/2,\,5/2}$ states through infrared transitions between 850 and 866 nm is possible. The transition frequencies can be determined through resonance fluorescence spectroscopy.

Collinear laser spectroscopy (CLS) is usually used to determine isotope shifts and hyperfine structures [1,37–41] but can also be used to determine transition frequencies [42–50]. In CLS, the compression of the velocity distribution upon electrostatic acceleration is utilized to yield fluorescence spectra with linewidths of the order of the natural linewidth. Due to the Doppler effect, the laser frequency needs to be shifted to match the resonance condition, depending on the geometry [collinear (c) or anticollinear (a)] and the unknown ion velocity. Consider a transition frequency ν_0 between an initial (i) and final (f) electronic state. When an ion is moving relative to the laboratory frame, ν_0 can be written as

$$\nu_0 = \nu_{lab}\gamma(1 - \beta\cos\alpha) = \begin{cases} \nu_c\gamma(1 - \beta) & \alpha = 0 \\ \nu_a\gamma(1 + \beta) & \alpha = \pi, \end{cases} \quad (3)$$

where $\gamma = 1/\sqrt{1 - \beta^2}$ is the time-dilation factor, $\beta = v/c$ is the ion velocity, and ν_{lab} and α are the transition frequency and the angle between the wave vector of the laser and the
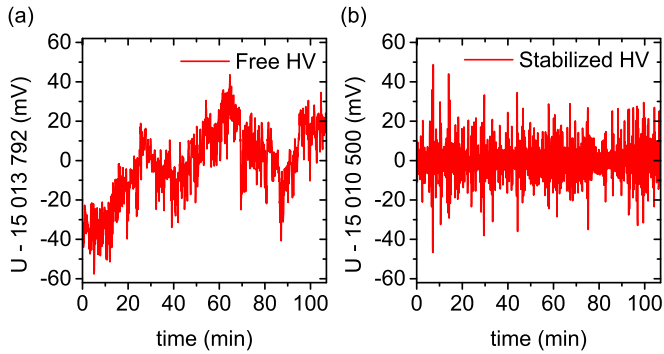
FIG. 1. Demonstration of the high-voltage stabilization to a high-voltage divider. (a) Without stabilization the high voltage (HV) drifts up to 40 mV/20 min, which corresponds to a frequency shift of 0.9 MHz for the D1 and D2 lines. (b) The high-voltage stabilization results in a stable mean with respect to the stability of the high-voltage divider. Residual voltage variations are of the order of 10 mV.

velocity vector of the ions in the laboratory frame, respectively. By combining measurements in the collinear (ν_c, $\alpha = 0$) and anticollinear (ν_a, $\alpha = \pi$) geometry, the unknown velocity in Eq. (3) can be eliminated by multiplying both cases to give

$$\nu_0 = \sqrt{\nu_c \gamma (1 - \beta) \nu_a \gamma (1 + \beta)} = \sqrt{\nu_c \nu_a}. \quad (4)$$

Hence ν_0 can be derived solely from the laser frequencies of the anticollinear/collinear alignment at resonance and equal ion velocities. However, a single photon recoil $\delta\nu_{rec} \approx h\nu_0^2/(2mc^2)$, representing the excess energy with respect to the difference in the energies of the electronic states ($E_f - E_i$) required for momentum conservation in the absorption process, has to be subtracted from Eq. (4), yielding

$$\nu_0 := (E_f - E_i)/h = \sqrt{\nu_c \nu_a} - \delta\nu_{rec}. \quad (5)$$

III. EXPERIMENT

An extensive description of the COALA setup is provided in Ref. [34]. The performance of this CLS setup was demonstrated in previous transition frequency measurements of Ba$^+$ [31] where accuracies of about 200 kHz were achieved. Several improvements were made to COALA for the measurements of Ca$^+$, which is considerably lighter than Ba and therefore more prone to systematic influences by, e.g., voltage variations, photon recoils, or the ion source temperature.

Ca$^+$ ions are produced and accelerated in a surface ionization source floated on an electrostatic potential of 15 kV relative to ground potential. An active stabilization to a precision high-voltage divider {Julie Research, HVA100, calibrated 2019 against Karlsruhe Tritium Neutrino (KATRIN) high-voltage (HV) divider [51]} using a digital feedback loop provides an ion source potential with relative variations of less than 1 ppm and negligible long-term drifts over the course of all measurements used to derive a single transition frequency. A comparison of the free-running and the stabilized high voltage is depicted in Fig. 1. In our quasisimultaneous approach collinear (c) and anticollinear (a) spectra are recorded consecutively following the scheme a-c-c-a. An individual spectrum of ^{40}Ca$^+$ took 1–2 min to record, whereas in the case of ^{46}Ca$^+$

the spectra were accumulated for 30–90 min to compensate for the smaller abundance. Switching between the different measurement geometries is effectively instantaneous for the D1 and D2 lines since two laser systems are available that are tuned to the collinear and the anticollinear resonance condition, respectively. In the case of infrared transitions, it takes roughly 3 min to adjust the laser frequency manually since the other laser system is occupied for optically transferring population into the metastable 3d states. In both cases, this means that slow monotonic drifts in the high voltage have negligible effect on the determined frequency whereas fluctuations as in Fig. 1(a) would result in a scattering of the data.

The beam of accelerated Ca$^+$ ions contains all stable isotopes according to their natural abundances. The ion beam is deflected by 10° to be superimposed with a laser in collinear or anticollinear geometry. Two electrostatic xy steerers, a quadrupole doublet and an einzel lens, enable alignment and collimation of the ion beam. A fluorescence detection region (FDR) is used to detect fluorescence photons and consists of two separate chambers, located directly next to each other along the beam axis [52]. In each chamber, fluorescence light emitted from the beam axis is focused into the second focal line of an elliptically shaped mirror and transferred onto a photomultiplier tube by a compound parabolic concentrator with an acceptance angle of 20° (CPC20) in the first and 30° (CPC30) in the second chamber. The FDR is floated on a voltage which is typically varied by 2–3 V to scan a resonance line by utilizing the Doppler effect. By changing the velocity of the ions, the laser frequencies can be fixed in the laboratory frame but are scanned in the rest frame of the ions with a differential Doppler factor of 22 MHz/V for the D1 and D2 lines and 10–12 MHz/V for the infrared lines. The voltage is supplied by an 18-bit digital-to-analog converter (DAC) generating voltages between −10 and 10 V, which is amplified by a factor of 50.2619(1) with a Kepco BOP-500M. Two diagnostic stations inside the beamline at a distance of 2.6 m, each equipped with an iris aperture, a Faraday cup, and a phosphor screen, facilitate proper alignment of the ion beam and the laser beams.

Continuous-wave laser light is produced by two Millennia eV Nd:YAG diode-pumped solid-state lasers (Spectra Physics), each pumping a narrow-band Matisse 2 TS Ti:sapphire ring laser (Sirah Lasertechnik). Both lasers can be frequency doubled with a WaveTrain 2 (Spectra Physics) using a lithium triborate (LBO) nonlinear crystal to produce coherent light at wavelengths of 397 and 393 nm to excite the D1 and D2 transitions, respectively. Both Ti:sapphire lasers are frequency stabilized with an FC1500-250-WG frequency comb (Menlo Systems), which is also used to measure the laser frequencies. A fraction of the laser light of the Ti:sapphire lasers is superimposed with a tooth of the frequency comb to generate a beat note. The beat note is fixed at 60 MHz by controlling the laser frequency via a digital feedback loop to its reference cavity, corresponding to a direct stabilization to the Global Positioning System (GPS)-disciplined quartz oscillator of the frequency comb. A frequency stability of 30 kHz on a timescale of minutes is reached with negligible long-term drifts. More information on the frequency stabilization and measurement can be found in our extended publication [34]. The linearly polarized
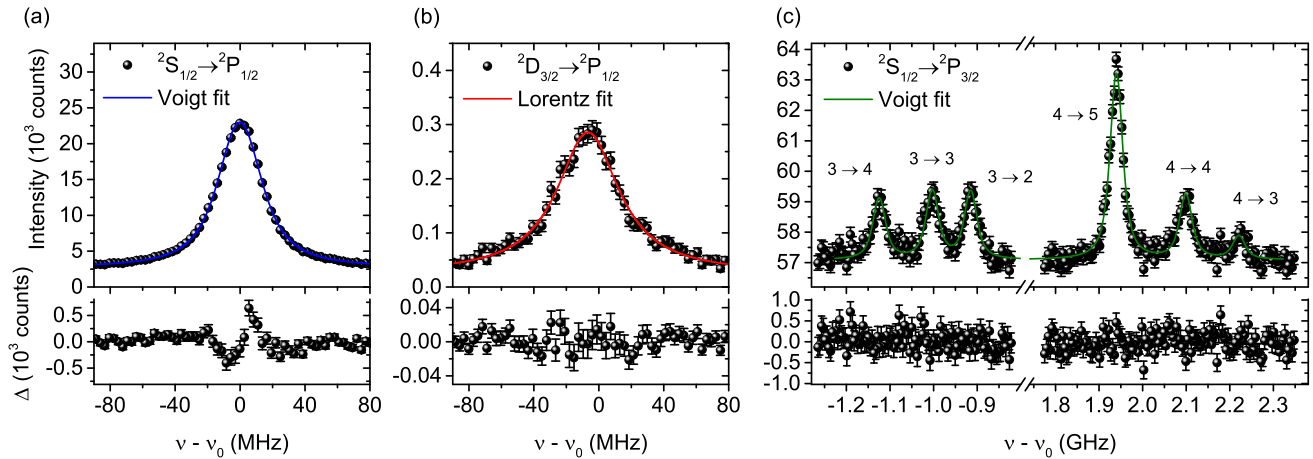
FIG. 2. Measured fluorescence spectra of the $4s\ ^2S_{1/2} \rightarrow 4p\ ^2P_{1/2}$ (D1) and $3d\ ^2D_{3/2} \rightarrow 4p\ ^2P_{1/2}$ lines of $^{40}Ca^+$. (a) Spectrum of the D1 line fitted with a symmetric Voigt profile. The fit residuals Δ reveal a small asymmetry in the line shape originating partly from the thermal velocity distribution in the ion source and photon recoils. (b) Spectrum of the infrared line fitted with a Lorentz profile. The linewidth corresponds to twice the natural linewidth of the $^2P_{1/2}$ state due to the optical population transfer. The laser background visible in the D1 spectrum vanishes for the infrared lines because of the insensitivity of the photomultiplier tubes to the infrared photons. (c) Fluorescence spectra of the $4s\ ^2S_{1/2} \rightarrow 4p\ ^2P_{3/2}$ (D2) lines of $^{43}Ca^+$. A sum of Voigt peaks using free intensity ratios is fitted to the data. The F quantum numbers for the lower and upper states are assigned to their corresponding peaks in the plot.

laser light is transported to COALA using optical single-mode fibers. Two mirrors in front of each entrance window allow one to adjust the position and angle of the lasers inside the beamline. The lasers are coupled back through their respective opposing fiber couplers to ensure an angular misalignment of less than 0.2 mrad. Electronic shutters are used for automated switching between the collinear and the anticollinear laser.

Spectroscopy of the $3d \rightarrow 4p$ transitions requires populating the $3d\ ^2D_{3/2}$ or $3d\ ^2D_{5/2}$ level. This is accomplished in an optical pumping drift tube with a length of 1.2 m in front of the FDR. It is floated on a small offset voltage of 27 V to spatially constrain the population transfer induced by the resonant pump laser that drives either the D1 or D2 transition. During these measurements, a triangular voltage modulation is applied to the starting potential to generate a 15-V broad and equally populated velocity distribution. In the pumping process, the velocity of the pumped ions is fundamentally defined by the chosen laser frequency with respect to the transition frequency. The velocity distribution of the pumped ions is determined by the natural linewidth of the respective $4p$ state of 23.05(9) MHz (D1) [53] and 23.97(15) MHz (D2) [54]. This corresponds to a Doppler-tuning width of about 2 V, which is much smaller than the artificial broadening. Thus asymmetries caused by optical pumping into the initial velocity distribution are strongly suppressed.

The laser light for probing the infrared transitions is provided by the second Ti:sapphire ring laser, which has to be used for both the collinear and anticollinear geometry. Excitation of a $3d \rightarrow 4p$ transition inside the FDR leads to deexcitation into the ground state and the emission of a UV photon, which can be readily detected with a photomultiplier tube. However, since the artificial broadening of the velocity distribution results in a smaller number of ions per velocity class, background suppression is even more important than in the spectroscopy of the D1 and D2 transitions. The laser for optical pumping was therefore switched off with

an acousto-optic modulator (AOM) with a rate of 37 kHz. Laser background-free fluorescence was observed only within a travel time of 7 μs following each pulse.

IV. RESULTS

A. Spectra of Ca$^+$

Spectra of the D1 and D2 lines were taken in the isotopes $^{40,42,43,44,46,48}Ca^+$, and spectra of the three $3d \rightarrow 4p$ lines were taken in $^{40,42,44,48}Ca^+$. As shown in Fig. 2, three fundamentally different cases occur: probing from the ground state of the isotopes with even mass number [Fig. 2(a)], pumping into and probing from the metastable $3d$ states [Fig. 2(b)], and probing from the ground states of the hyperfine structure (HFS) of $^{43}Ca^+$ [Fig. 2(c)].

When probing from ground states, the observed resonance is a convolution of the initial velocity distribution with the transition line shape. In some measurements a second peak occurred in the fluorescence spectrum presumably due to a second ionization spot inside the ion source leading to an additional systematic uncertainty contribution which will be explained in Sec. IV B. However, in later measurements this second peak was eliminated by using a tantalum inlet inside the graphite oven of the ion source. In Fig. 2(a), a spectrum of the D1 line of $^{40}Ca^+$ under the latter conditions is shown. A symmetric Voigt profile was fitted to the data to account for Gaussian broadening originating from voltage variations in the source. The full width at half maximum (FWHM) of $\Gamma = 32.63(78)$ of the depicted resonance peak, with $\Gamma_L = 26.15(56)$ MHz and $\Gamma_G = 14.13(82)$ MHz for the Lorentzian and the Gaussian part, respectively, is only slightly larger than the natural linewidth of 23.05(9) MHz [53]. In the case of spectra with side peak, a satellite peak is included in the fit routine, yielding the same linewidth. The remaining small asymmetry is ascribed to the velocity distribution of the ions inside the source as described by Kretzschmar *et al.* [55].

TABLE I. Transition frequencies of the $4s\ ^2\mathrm{S}_{1/2} \rightarrow 4p\ ^2\mathrm{P}_{1/2}$ (D1) and $4s\ ^2\mathrm{S}_{1/2} \rightarrow 4p\ ^2\mathrm{P}_{3/2}$ (D2) transition in $^A\mathrm{Ca}^+$ ions. For each isotope and transition, the number in the first parentheses denotes the systematic uncertainty, whereas that in the second denotes the total uncertainty. The literature values for the D1 and D2 lines in $^{40}\mathrm{Ca}^+$ are taken from Wan *et al.* [27] and Shi *et al.* [11], respectively. The literature values of the other isotopes were calculated with the corresponding isotope shifts from Gebert *et al.* [28] and Shi *et al.* [11] as well as from Mårtensson-Pendrill *et al.* [59] and Garcia Ruiz *et al.* [15] for $^{43,46}\mathrm{Ca}^+$. All values are in megahertz.

A	ν^A_{D1} (this work)	ν^A_{D1} (Refs. [27,28,59])	ν^A_{D2} (this work)	ν^A_{D2} (Refs. [11,15])
40	755 222 765.66(10)(10)	755 222 765.896(88)	761 905 012.53(11)(11)	761 905 012.599(82)
42	755 223 191.15(10)(10)	755 223 191.602(129)	761 905 438.57(9)(10)	761 905 438.531(108)
43	755 223 443.57(14)(30)	755 223 438(15)	761 905 691.89(10)(17)	761 905 695.6(2.8)
44	755 223 614.66(10)(10)	755 223 615.430(115)	761 905 862.62(9)(9)	761 905 862.830(105)
46	755 224 063.27(23)(33)	755 224 053(12)	761 906 311.60(22)(57)	761 906 313.6(3.6)
48	755 224 471.12(9)(10)	755 224 471.285(107)	761 906 720.11(9)(11)	761 906 720.544(106)

Its impact on the rest-frame frequency determination cancels in the collinear/anticollinear approach. Another possible explanation, photon recoils which occur more frequently in the peak center, is considered as a systematic uncertainty.

Spectra of the $3d \rightarrow 4p$ transitions can be fitted sufficiently with a simple Lorentz profile, since they require optical pumping before they can be recorded with the probe laser. As mentioned in Sec. III, ions are pumped from an equally populated velocity distribution. A spectrum of the $^2\mathrm{D}_{3/2} \rightarrow {}^2\mathrm{P}_{1/2}$ transition is shown in Fig. 2(b). The shape of the spectrum corresponds to a Lorentz profile whose FWHM of 46.5(1.7) MHz corresponds to twice the natural linewidth [46.10(14) MHz] of the intermediate $^2\mathrm{P}_{1/2}$ state from pumping and probing.

A special case is the isotope $^{43}\mathrm{Ca}^+$, which is the only stable isotope with a HFS splitting. A spectrum of the D2 line in $^{43}\mathrm{Ca}^+$ is shown in Fig. 2(c). $^{43}\mathrm{Ca}^+$ has a nuclear spin of $I = 7/2$ giving rise to a magnetic dipole term in the splitting of the $^2\mathrm{S}_{1/2}$, $^2\mathrm{P}_{1/2}$, and $^2\mathrm{P}_{3/2}$ states as well as an additional electric quadrupole term in the latter case. Moreover, quantum interference (QI) effects can appear in the spectrum of the D2 line, which would lead to small asymmetries and varying peak intensities, depending on the polarization of the spectroscopy light and the fluorescence detection geometry used [56–58]. The influence of QI on fluorescence spectra was investigated elaborately and proven in specialized measurements with a modified FDR, which will be reported elsewhere. Due to the 4π coverage of the FDR [52] used for the measurements described here, QI effects are strongly suppressed and have no impact on the final result.

B. Determination of the transition frequency ν_0

The measured laser frequencies $\nu_{\mathrm{c/a}}$ and the measured voltage difference δU between the peak positions of a collinear and an anticollinear spectrum are used to determine the rest-frame transition frequency ν_0. Since the laser frequencies cannot be adjusted perfectly such that both peaks appear at the same voltage, a small correction for the difference δU has to be applied to Eq. (5) such that

$$\nu_0 = \sqrt{\nu_{\mathrm{c}}\left(\nu_{\mathrm{a}} - \frac{\partial \nu_{\mathrm{a}}}{\partial U}\delta U\right)} - \delta\nu_{\mathrm{rec}}, \qquad (6)$$

where $\partial\nu_{\mathrm{a}}/\partial U = -\nu_{\mathrm{a}}q/(\beta\gamma mc^2)$ is the differential Doppler factor. The recoil shift $\delta\nu_{\mathrm{rec}}$ amounts to 32 kHz for the D1 and D2 lines and 7 kHz for the three infrared transitions.

The results of the transition frequency evaluation are compiled in Tables I–IV for the $4s \rightarrow 4p$ and $3d \rightarrow 4p$ transitions. An elaborate analysis of the systematic uncertainties of the transition frequency measurements was carried out. Resulting from the natural abundances of the isotopes and the addressability of the spectral line, the statistical uncertainty plays a minor role in the D1 and D2 lines of $^{40,42,44,48}\mathrm{Ca}^+$ and in the $3d \rightarrow 4p$ transitions of $^{40}\mathrm{Ca}^+$, while it is dominant or of the same order of magnitude as the systematic uncertainty in the remaining cases. The uncertainty contributions for the measured transitions are compiled in Table V for $^{40}\mathrm{Ca}^+$ and $^{43}\mathrm{Ca}^+$. The systematic uncertainties for the remaining isotopes do not differ fundamentally from those of $^{40}\mathrm{Ca}^+$. The main contributions to the systematic uncertainties in the D1 and D2 lines are photon recoils in the FDR in the case of multiple excitations, the uncertainty of the overlap and collimation of the ion and laser beams, and deviations from a symmetric line shape:

(i) During the evaluation of the spectroscopy data, particular care was taken for photon recoils in the FDR. Since the number of possible photon absorptions during the probing process heavily depends on the intensity of the laser light, which was changed between different measurement days, an individual systematic uncertainty was assigned to each series of measurements. The mean number of photon absorptions was estimated using the equilibrium scattering rate of a two-level atom inside a coherent radiation field and the interaction time between laser and ions inside the FDR.

(ii) Similarly, the uncertainty due to the appearance of a satellite peak in some of the spectra of the D1 and D2 lines was used only if the second peak occurred. This second peak was found to originate from a second ionization spot inside the ion source, which combined with a voltage gradient of roughly 4 V along the ionization chamber led to a second velocity class. However, since when fitting with a sum of two Voigt profiles small deviations in the residuals were still visible, a systematic uncertainty was estimated by comparing the results after using both peaks for the evaluation. In later measurements the satellite peak was eliminated by using tantalum instead of graphite as the ionization surface material,

TABLE II. Isotope shifts of the $4s\,{}^2S_{1/2} \rightarrow 4p\,{}^2P_{1/2}$ (D1) and $4s\,{}^2S_{1/2} \rightarrow 4p\,{}^2P_{3/2}$ (D2) transition in ${}^ACa^+$ ions relative to ${}^{40}Ca^+$. Our isotope shifts are calculated using the transition frequencies from Table I. The literature values are from Gebert *et al.* [28] and Shi *et al.* [11] as well as from Mårtensson-Pendrill *et al.* [59] and Garcia Ruiz *et al.* [15] for ${}^{43,46}Ca^+$. All values are in megahertz.

A	$\delta\nu_{D1}^{40,A}$ (this work)	$\delta\nu_{D1}^{40,A}$ (Refs. [28,59])	$\delta\nu_{D2}^{40,A}$ (this work)	$\delta\nu_{D2}^{40,A}$ (Refs. [11,15])
42	425.49(15)	425.706(94)	426.04(15)	425.932(71)
43	677.91(32)	672(15)	679.36(20)	683.0(2.8)
44	849.00(14)	849.534(74)	850.09(14)	850.231(65)
46	1297.61(34)	1287(12)	1299.07(58)	1301.0(3.6)
48	1705.46(14)	1705.389(60)	1707.58(16)	1707.945(67)

benefiting from its lower electric resistance and hence smaller voltage gradient. A direct comparison between the measurements with symmetric spectra and those with satellite peak yielded deviations of the order of the estimated uncertainty of the double-peak spectra.

(iii) The systematic uncertainty due to tilts between the two laser beams and the ion beam was calculated by averaging the Doppler shift over all possible angle pairs if assuming a maximum tilt of 0.2 mrad between the laser beams and 1 mrad between the ion beam and the maximally tilted laser beam. The first limit is an estimation for which both lasers still pass their respective opposing fiber coupler standing 7 m apart, whereas the second limit was estimated by considering the two iris apertures inside the beamline at a distance of 2.6 m with an opening diameter of 5 mm and the ion beam, which has a diameter of 3 mm. Frequency shifts caused by the wave-front curvature are estimated to be of the order of about 40 kHz but cancel almost completely in the collinear/anticollinear approach. Thus they are neglected in the final uncertainty.

(iv) The systematic uncertainty due to an insufficiently collimated ion or laser beam was determined experimentally by changing the focusing settings of the ion optics or the fiber couplers, respectively. Supplementarily, changing the diameter of the two iris apertures inside the beamline to test the influence of the overlap between ion and laser beam(s) gave rise to another systematic uncertainty contribution.

(v) A small asymmetry in the fluorescence spectra originating partly from the acceleration of thermally distributed ions leads to a shift of the peak position and was investigated using a line-shape model developed in Ref. [55]. Again, the asymmetry is inverted between the collinear and anticollinear geometry, and their effects largely cancel in the determined transition frequency. The additional uncertainty of 23 kHz is considerably smaller than the other uncertainties.

For ${}^{43}Ca^+$, the influence of QI on the hyperfine spectrum of the D2 line was investigated elaborately. Although QI effects were proven in systematic measurements, they are suppressed in our experiment due to the geometry of the FDR, which collects a solid angle close to 4π around the emitted fluorescence light. Additionally, deviations in the baseline of the hyperfine spectrum of ${}^{43}Ca^+$ were considered in the systematics. More precisely, the laser-induced background was constant within the peak doublet (D1) or triplet (D2) corresponding to the hyperfine structure of the excited states but differed between the two ground states. For the determination of transition frequencies, the background was adjusted during evaluation to be constant across the entire spectrum. The estimation of the uncertainty was done by systematically shifting the two background base lines against each other and comparing the results.

For the measurements of the $3d \rightarrow 4p$ transitions in the even Ca^+ isotopes, the systematic uncertainties from the satellite peak and the acceleration of thermally distributed ions do not appear because of the optical pumping process. The systematic uncertainty due to photon recoils in the FDR can also be neglected since 93% of the probed ions end up in the ground state after one excitation and, furthermore, a single recoil for the corresponding wavelengths shifts the transition frequency by less than 10 kHz. However, in the $3d \rightarrow 4p$ transitions, systematic frequency shifts from photon recoils in the optical pumping region which become visible

TABLE III. Transition frequencies $\nu_{J\rightarrow J'}^A$ of the $3d\,{}^2D_J \rightarrow 4p\,{}^2P_{J'}$ transitions in ${}^ACa^+$ ions. For each isotope and transition, the number in the parentheses denotes the total uncertainty, whereas the systematic uncertainties for our results amount to 130 kHz. The literature values for the ${}^2D_{3/2} \rightarrow {}^2P_{1/2}$ line in ${}^{40}Ca^+$ are taken from Gebert *et al.* [28], and those of the ${}^2D_{3/2,5/2} \rightarrow {}^2P_{3/2}$ lines are taken from Götte *et al.* [48]. The literature values of the other isotopes were calculated with the isotope shifts from Gebert *et al.* [28] and Nörtershäuser *et al.* [60], respectively. All values are in megahertz.

A	$\nu_{3/2\rightarrow1/2}^A$ (this work)	$\nu_{3/2\rightarrow1/2}^A$ (Ref. [28])	$\nu_{3/2\rightarrow3/2}^A$ (this work)	$\nu_{3/2\rightarrow3/2}^A$ (Ref. [48,60])	$\nu_{5/2\rightarrow3/2}^A$ (this work)	$\nu_{5/2\rightarrow3/2}^A$ (Ref. [48,60])
40	346 000 235.13(14)	346 000 234.867(96)	352 682 481.93(13)	352 682 480.2(5.8)	350 862 882.63(13)	350 862 880.8(5.3)
42	345 997 884.98(30)	345 997 884.893(138)	352 680 132.39(31)	352 680 128.0(6.2)	350 860 536.90(27)	350 860 530.4(6.8)
44	345 995 736.34(30)	345 995 735.984(125)	352 677 984.50(26)	352 677 981.5(6.5)	350 858 392.30(26)	350 858 385.6(6.8)
48	345 991 937.64(28)	345 991 937.098(126)	352 674 186.53(37)	352 674 182.5(8.2)	350 854 600.00(21)	350 854 593.0(8.8)

TABLE IV. Isotope shifts $\delta\nu_{J\to J'}^{40,A}$ of the $3d\,^2D_J \to 4p\,^2P_{J'}$ transitions in ^{A}Ca$^+$ ions relative to ^{40}Ca$^+$. Our isotope shifts are calculated using the transition frequencies from Table III. The literature values are from Gebert *et al.* [28] and Nörtershäuser *et al.* [60]. All values are in megahertz.

A	$\delta\nu_{3/2\to 1/2}^{40,A}$ (this work)	$\delta\nu_{3/2\to 1/2}^{40,A}$ (Ref. [28])	$\delta\nu_{3/2\to 3/2}^{40,A}$ (this work)	$\delta\nu_{3/2\to 3/2}^{40,A}$ (Ref. [60])	$\delta\nu_{5/2\to 3/2}^{40,A}$ (this work)	$\delta\nu_{5/2\to 3/2}^{40,A}$ (Ref. [60])
42	−2350.15(33)	−2349.974(99)	−2349.54(34)	−2352.2(2.1)	−2345.73(30)	−2350.4(4.3)
44	−4498.79(33)	−4498.883(80)	−4497.43(29)	−4498.7(3.0)	−4490.33(29)	−4495.2(4.3)
48	−8297.49(31)	−8297.769(81)	−8295.40(39)	−8297.7(5.8)	−8282.63(25)	−8287.8(7.0)

in time-resolved spectra have to be considered. During the time interval of 7 μs used for the observation of a $3d \to 4p$ resonance after a pumping cycle, the peak position shifts by about ±3 MHz, while recording a collinear or anticollinear spectrum, respectively. We assume that this originates from the fact that ions which contribute to the fluorescence spectrum at the end of the recording time interval have had a shorter interaction time with the chopped pump laser and hence experienced fewer photon recoils. Moreover, variations in both the ion and laser beam diameter along the pumping drift tube might lead to an amplification of this effect and additionally to variations in the effective Doppler shift across the pumping region. Although these effects are of opposite sign for collinear and anticollinear spectra, a residual shift by about 100 kHz during the recording time interval was found, which is actually the dominant systematic uncertainty of these lines.

TABLE V. Typical uncertainty contributions in the spectroscopy of even (here, ^{40}Ca$^+$) and odd isotopes (^{43}Ca$^+$). These were determined for each individual line and isotope. However, there are only three cases which have to be distinguished fundamentally and are shown exemplarily in the three columns. The contributions include frequency shifts due to photon recoils in the FDR as well as during optical pumping ($3d \to 4p$) and the influence of the Doppler effect due to tilted laser beams, collimation quality of ion and laser beam(s), and overlap of the beams. Moreover, the influence of the line-shape model due to the acceleration of thermally distributed ion ensembles and the appearance of a satellite peak in some of the spectra was considered. In particular, for ^{43}Ca$^+$, QI effects (D2) and differing background heights between the peaks of the two ground states' components are included. All values are in kilohertz.

Contribution	^{40}Ca$^+$ D1/D2	^{40}Ca$^+$ $3d \to 4p$	^{43}Ca$^+$ D1/D2
Photon recoils	57	0	41/32
Tilt ∡(laser, laser)	17	12	16/17
Collimation (laser, ions)	51	51	51
Beam overlap	47	47	47
Satellite peak	30/51	0	16/18
Thermal ion ensemble	23	0	23
Quantum interference	0	0	0/12
Inconstant background	0	0	103/53
Optical pumping	0	105	0
Systematics	99/107	126	135/100
Statistics	5/7	57	270/136
Total	99/107	138	302/169

V. DISCUSSION

A. Transition frequencies

A consistency check of the determined transition frequencies was carried out by combining a set of frequencies $(\nu_i^A)_{i\in\mathcal{I}}$ with each other through addition and subtraction such that the expectation value $\mathbb{E}$ of the total operation is zero since it starts and ends in the same level; hence

$$\mathbb{E}\left[\sum_{i\in\mathcal{I}} \pm \nu_i^A\right] = 0. \tag{7}$$

Such "ring closures" are of particular interest, because the data provided here can be combined with precisely determined transition frequencies of other groups. The ring closures across the energy states of Ca$^+$ investigated here are illustrated in Fig. 3 together with the results for the different isotopes shown besides the level scheme. In five of the six rings, literature values of the $4s\,^2S_{1/2} \to 3d\,^2D_{5/2}$ or the $3d\,^2D_{3/2} \to 3d\,^2D_{5/2}$ transition with hertz-level precision were used for the closure. The former of these electric-dipole-forbidden transitions was measured by Chwalla *et al.* [61] as well as Guan *et al.* [62], and additional isotope shift measurements are from Knollmann *et al.* [64]. The latter transition was measured by Solaro *et al.* [63,65]. Since these two transitions were measured with a precision at the hertz level, they do not introduce additional uncertainties into the ring closures. The total uncertainty of the ring closures was calculated using Gaussian error propagation.

All ring closures shown in Fig. 3 were calculated for the isotopes ^{40,42,44,48}Ca$^+$. The expectation value of zero lies at least within the 1.5σ uncertainty of every considered ring closure. However, the majority (75%) agrees within the 1σ uncertainty, well in accordance with statistical expectations. This strongly indicates the consistency of our measurements with our own and external data, which supports the quality of the field-shift ratio that is derived from this data. The consistency of these ring closures is also the main argument why the previous ion-trap measurements are thought to be affected with a small additional systematic uncertainty as discussed in the next section.

B. Field-shift ratios

A King-plot analysis was carried out to determine the field-shift ratio F_{D2}/F_{D1} which gave rise to the Ca$^+$ field-shift puzzle [11]. Measuring transition frequencies allows an easy redefinition of the reference isotope ^{A}Ca$^+$ without introducing additional uncertainties. Therefore a total of six King plots were carried out to determine a mean field-shift ratio
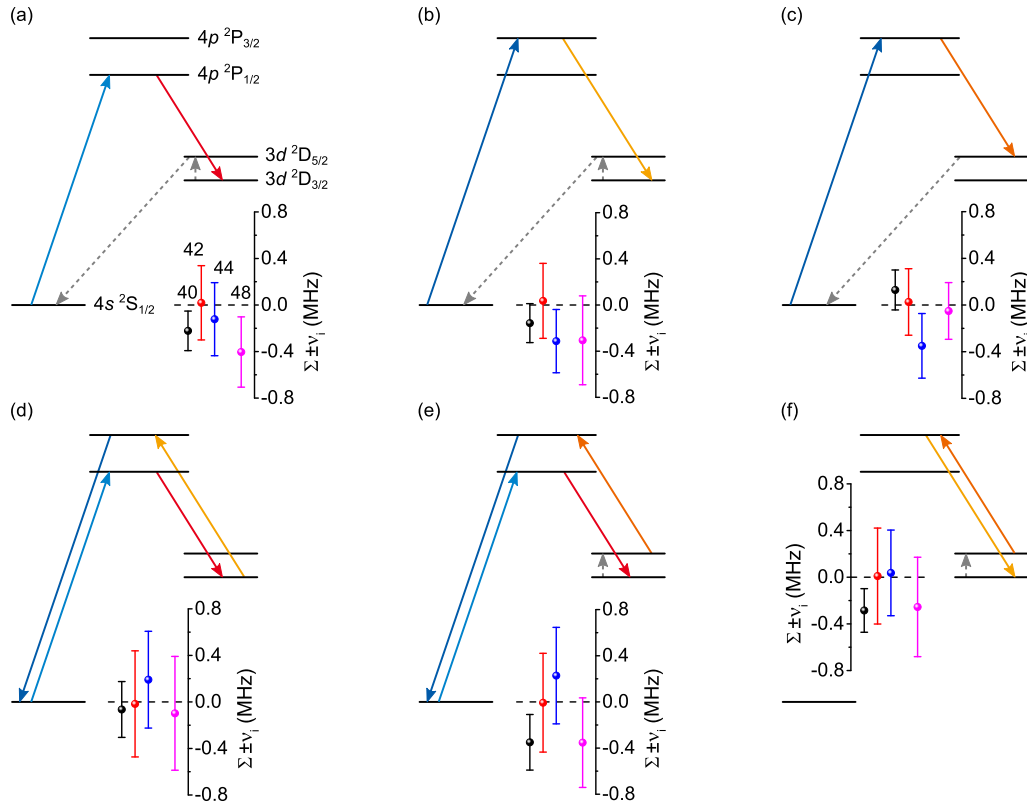
FIG. 3. Ring closures across the energy states of ^{40,42,44,48}Ca$^+$. (a)–(c) include one $4s \to 4p$ and one $3d \to 4p$ transition, whereas (d)–(f) include an even number of each. Moreover, the ring closures in (d)–(f) can be calculated by subtracting two of the ring closures from (a)–(c) from each other. The transition frequencies of the electric-dipole-forbidden $4s\ ^2S_{1/2} \to 3d\ ^2D_{5/2}$ and $3d\ ^2D_{3/2} \to 3d\ ^2D_{5/2}$ transitions were taken from Chwalla *et al.* [61] and Guan *et al.* [62] and from Solaro *et al.* [63], respectively. Isotope shifts of these transitions are from Knollmann *et al.* [64] and Solaro *et al.* [65].

which has an increased robustness against statistical outliers, and the weighted mean of the determined field-shift ratios was taken as the final result. Since these are all based on the same data set, they are not statistically independent, and the uncertainty was estimated conservatively by taking the standard error of the weighted mean under the assumption of positive correlation. Thus, pairwise, the field-shift ratios have a correlation coefficient of 1. The modified isotope shifts $\mu\delta\nu_i^{A,A'}$ were calculated with the nuclear masses by using the atomic masses reported in Atomic Mass Evaluation 2016 [66], subtracting 20 electron masses, and adding their total binding energy. The King plot for the case of the "natural" reference isotope ^{40}Ca$^+$ is depicted in Fig. 4 together with the linear fit from Shi *et al.* [11]. The slope of our fit of $F_{D2}/F_{D1} = 1.0010(23)$ is significantly smaller than the previous value of 1.0085(12). In Table VI, the field-shift ratio F_{D2}/F_{D1} and the y-axis offset $K_{D2} - K_{D1}(F_{D2}/F_{D1})$ are listed for the different reference isotopes. Our y-axis offset of 0.09(95) GHz u is not significantly different from zero, contrary to the value of $-2.873(473)$ GHz u obtained in Ref. [11], which is also a consequence of the smaller field-shift ratio. All even-even isotopes agree within the 0.5σ region with the King fit, but ^{43}Ca$^+$ lies only within 1.5σ as indicated by the inset plot in Fig. 4. We are assuming that this deviation is due to statistics rather than having a physical reason. Performing the King-plot analysis without ^{43}Ca$^+$ shifts the field-shift ratio to 1.0008(22)

and the y-axis offset to 0.18(91). Hence ^{43}Ca$^+$ qualitatively does not change our results.

A comparison of these experimental results with the theoretical values obtained in Ref. [11] is shown in Fig. 5. The new experimental value agrees well with theoretical predictions of a mean-field approach which uses Dirac-Fock calculations, both without and with considering core polarization (DF and DF Core Pol., respectively) [11], as well as with results from

TABLE VI. The field-shift ratio F_{D2}/F_{D1} and the y-axis offset $K_{D2} - K_{D1}(F_{D2}/F_{D1})$ in GHz u for all measured reference isotopes. The final value is given by their weighted average. The uncertainty of the final value is given by the standard error of the (weighted) mean under the conservative assumption of positively correlated random variables.

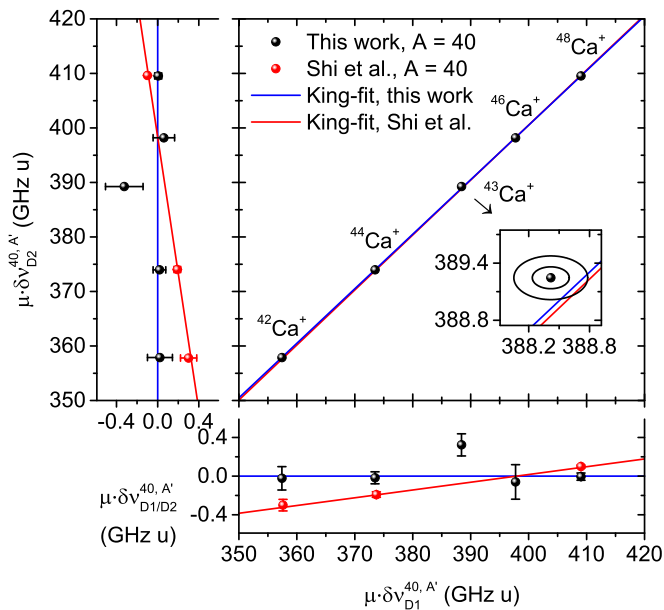| A_{ref}	F_{D2}/F_{D1}	$K_{D2} - K_{D1}(F_{D2}/F_{D1})$
40	1.0005(23)	0.33(92)
42	1.0013(24)	$-0.02(99)$
43	1.0012(52)	$-0.05(2.13)$
44	1.0013(17)	$-0.02(69)$
46	1.0012(93)	$-0.08(3.81)$
48	1.0007(25)	0.22(1.07)
Total	1.0010(23)	0.09(95)

FIG. 4. King plot of the D2 line against the D1 line with ^{40}Ca$^+$ as the reference isotope. The narrow plots with magnified axes on the left and the bottom of the main plot depict the deviations between the data and our fit concerning the x and the y axes. The regression line passes through the data points of all isotopes within the 0.5σ region with the exception of ^{43}Ca$^+$, where it is only within the 1.5σ region as indicated by the inset plot, which shows the 1σ and 2σ uncertainty regions for this isotope. The linear fit from Shi et al. [11] elucidates the discrepancy between their field-shift ratio and ours, which solves the Ca$^+$ field-shift puzzle. The fit accounts for both the uncertainties of the D1 and D2 lines as described by York et al. [67].

many-body perturbation theory [MBPT and configuration interaction combined with MBPT (CI+MBPT)] [11,68]. The previously obtained discrepancy is resolved. The field-shift ratio also reduces the field-shift contribution in the splitting isotope shift of the $4p\ ^2P_{1/2} \rightarrow 4p\ ^2P_{3/2}$ fine-structure transition to only 10% of the value reported in Ref. [11]. It is therefore smaller than the experimental uncertainty, and hence the field shift of the splitting isotope shift actually has not been detected yet, contrary to what was reported in Ref. [11].

In order to find the origin of the deviation between the experimental results, it is instructive to compare the isotope shifts directly. Figure 6 depicts those from Shi et al. [11] relative to our results. The experimentally determined isotope shifts of ^{48}Ca$^+$ in the D2 transition and, in particular, of ^{44}Ca$^+$ in the D1 transition differ significantly from each other. When comparing this figure with the enlarged small frames in Fig. 4, it is striking how well the isotope shifts are located along a line, even though the deviations in Fig. 6 do not look systematically shifted, especially not in the D1 line. Since the values in the King plot are multiplied by the mass factor, one may speculate that a mass-dependent effect is playing a role. The relatively large slope in the King plot of the previous measurements can therefore be traced back particularly to the differences in ^{42,44}Ca$^+$.

In order to gain more information on possible systematics in previous measurements, the ring closure depicted in Fig. 3(a) was calculated with the results of the D1 transition
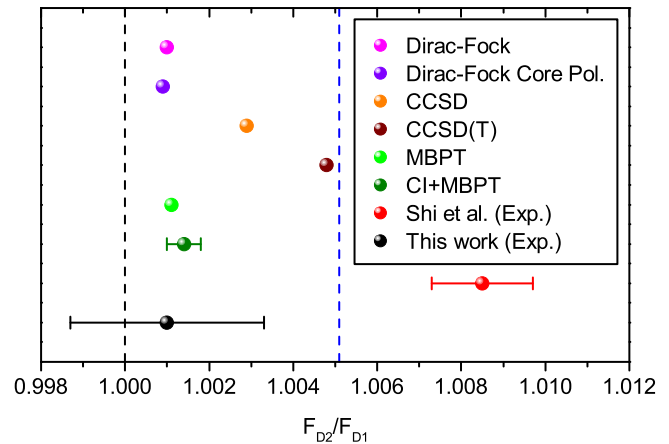

FIG. 5. Comparison of the field-shift ratio F_{D2}/F_{D1} between experiment and theory. The dashed lines represent the nonrelativistic (black) and the relativistic (blue) limit. Whereas the previous experimental value from Shi et al. [11] exceeds the relativistic limit of 1.0051, our result is consistent with the given limits and agrees with most of the theories. CCSD, coupled-cluster theory with single and double excitations; CCSD(T), coupled-cluster theory with single, double, and partially triple excitations; Exp., experiment.

from Wan et al. [27] and the isotope shift measurements from Gebert et al. [28]. The results are shown in Fig. 7. Besides those of ^{48}Ca$^+$, the closures significantly deviate (2.1σ, 2.1σ, and 6.8σ for ^{40,42,44}Ca$^+$) from the expectation value, indicating that the previously determined frequencies of the D1 line are too large or those of the $3d\ ^2D_{3/2} \rightarrow 4p\ ^2P_{1/2}$ transition are too small.

C. Nuclear charge radii

The authors of Refs. [11,28] used the isotope shifts to determine changes in the mean-square nuclear charge radii with improved precision. We followed the same procedure to study how strongly the differences in the measured isotope shifts affect the atomic factors and, consequently, the charge radii and to improve the values for ^{43,46}Ca$^+$ which were previously not measured with comparable accuracy. Therefore
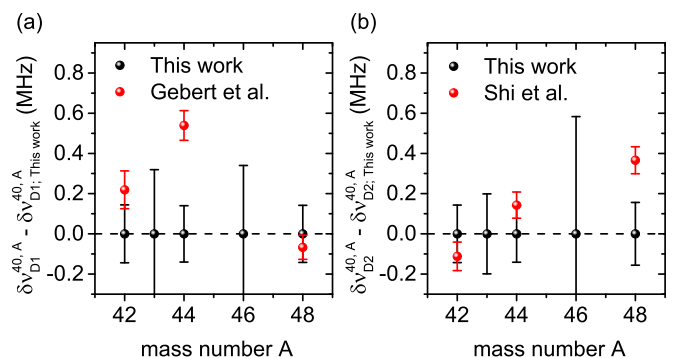

FIG. 6. Isotope shifts (a) of the D1 line from Gebert et al. [28] and (b) of the D2 line from Shi et al. [11] relative to our results. A large discrepancy was found for the D1 line in ^{44}Ca$^+$, which together with the linear trend in the D2 line explains the difference between the field-shift ratio from Shi et al. and this work.
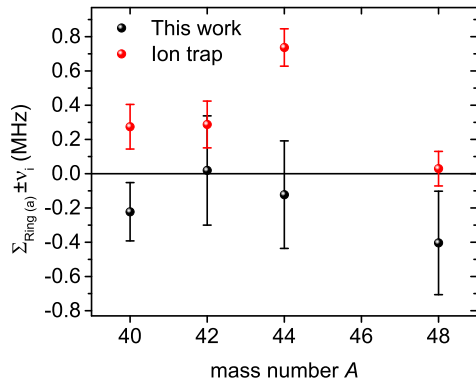
FIG. 7. Comparison of ring closure from Fig. 3(a) between our results and the results of the previous trap measurements from Wan *et al.* [27] (^{40}Ca$^+$) and Gebert *et al.* [28] (^{42,44,48}Ca$^+$). The expected value of the ring closure for each isotope is 0 MHz. Whereas our results all agree with the expected value at least within 1.5σ, the literature values for ^{40,42}Ca$^+$ both deviate by 2.1σ, and the result for ^{44}Ca$^+$ even deviates by 6.8σ. Only ^{48}Ca$^+$, whose isotope shift was closest to our result, agrees with the expectation value.

we have used the changes in the mean-square nuclear charge radii $\delta\langle r^2\rangle^{A,A'}$ extracted from muonic atom spectroscopy data and elastic electron scattering, compiled in Ref. [69]. This is the latest compendium; it considers all previous publications and provides a uniform treatment of all chemical elements for which data from muonic atoms are available. Note that in the previous studies [11,28] these data were taken from Ref. [18], which yields slightly different $\delta\langle r^2\rangle^{A,A'}$.

Performing a linear regression with the modified isotope shifts obtained in this paper plotted against the modified $\delta\langle r^2\rangle^{A,A'}$ yields the field- and mass-shift constants that can be used subsequently to calculate improved $\delta\langle r^2\rangle^{A,A'}$ values from the isotope shifts; cf. Eq. (1). For the fitting, the algorithm of York *et al.* [67] was used with the addition of an integer parameter α which shifts the x axis of the plot to remove the correlation between the two fitting parameters of the fit as described by Hammen *et al.* [70]. The results of this King-plot analysis are compiled in Table VII.

The field-shift constants resulting from our isotope shifts of the D1 and D2 lines are much closer than those from Refs. [11,28], reflecting the smaller field-shift ratio discussed above. The small differences in the other fit parameters are almost exclusively caused by the different basis of $\delta\langle r^2\rangle^{A,A'}$, which was confirmed by using the data from Ref. [18] in our analysis. In this case, besides F all fit parameters and optimized $\delta\langle r^2\rangle$ values are practically coincident with those obtained in the trap.

VI. CONCLUSION

The $4s \rightarrow 4p$ and $3d \rightarrow 4p$ transition frequencies were measured for ^{40,42,43,44,46,48}Ca$^+$ and ^{40,42,44,48}Ca$^+$, respectively, with an accuracy of up to 100 kHz with quasisimultaneous collinear/anticollinear laser spectroscopy. An elaborate evaluation of the systematic uncertainties appearing at COALA was carried out, which enables us

TABLE VII. Field- and mass-shift constants of the D1 and D2 lines and optically improved nuclear charge radii. The field- and mass-shift constants correspond to the slope and y intercept of a linear fit to the relative mean-square nuclear charge radii from Ref. [69] plotted against the isotope shifts of the D1 or the D2 line according to Eq. (1). For the fitting, the algorithm by York *et al.* [67] was again utilized with the addition of the parameter α to reduce the uncertainties of the fits as described in Ref. [70]. The relative mean-square nuclear charge radii have been improved by evaluating the fit results with the isotope shifts determined in this paper. The two transitions were combined using the weighted average and its standard error for positively correlated random variables. F, K factors, α, and mean-square nuclear charge radii are given in MHz/fm^2, GHz u, fm^2 u, and fm^2, respectively.

Parameter	This work	Shi *et al.* [11]
F_{D1}	$-288.7(7.2)$	$-281.8(6.9)$
K_{D1}	$407.60(48)$	$408.73(40)$
α_{D1}	34	
F_{D2}	$-288.5(7.2)$	$-284.7(8.2)$
K_{D2}	$408.12(51)$	$409.35(42)$
α_{D2}	40	
$\delta\langle r^2\rangle^{40,42}$	$0.2071(44)$	$0.2160(49)$
$\delta\langle r^2\rangle^{40,43}$	$0.1149(29)$	
$\delta\langle r^2\rangle^{40,44}$	$0.2688(56)$	$0.2824(64)$
$\delta\langle r^2\rangle^{40,46}$	$0.1117(49)$	
$\delta\langle r^2\rangle^{40,48}$	$-0.0207(74)$	$-0.0045(59)$

to further reduce our systematic uncertainty, such that we effectively remain limited only by the quality of our ion beam. A successful check of self-consistency was carried out by considering "ring closures" with the measured transitions, which corroborates the quality of our results. Isotope shifts can be calculated between all addressed isotopes; we took advantage of this for the determination of the field-shift ratio F_{D2}/F_{D1}. A total of six correlated field-shift ratios were derived, whose weighted mean was taken as the final value.

Our experimental value $F_{D2}/F_{D1} = 1.0010(23)$ removes the discrepancy between atomic structure calculations and experiment reported in Ref. [11]. Comparing the ring closures of our measurements with those of the previous measurements leads to the assumption that the trap measurements were afflicted with a systematic but yet undiscovered influence. Since this systematic effect seems to preserve the linearity of the King plot, it could be a mass-related effect. The approach used in Refs. [11,27,28] has not been used for electric dipole transitions in other ion species so far. The experimental realization for laser spectroscopy on clock transitions in highly charged ions by Micke *et al.* [71] is considerably different, and conclusions on it cannot be drawn. However, it can be summarized that calculations with the Dirac-Fock equation [11] and many-body perturbation theory [68] suffice to describe the field-shift ratio in light to medium nuclei with alkalilike electronic configuration for the given experimental precision. Also, our previous measurements with Ba$^+$, which has a heavy nucleus, were in very good agreement with theory [31]. Measurements with Sr$^+$, which has four stable isotopes, would close the gap between Ca$^+$ and Ba$^+$ and complete

the experimental analysis of the field-shift ratio for the stable alkaline-earth metals.

Finally, a King-plot analysis with the nuclear charge radii from elastic electron scattering and muonic atom spectroscopy and our isotope shifts was carried out to determine the field- and mass-shift constants as well as improved mean-square nuclear charge radii. The results will also have significant influence on the combined analysis of all Ca$^+$ transitions presented in Ref. [33].

In the next step, measurements with similar precision on He-like systems of light isotopes are needed. Since laser spectroscopy in these systems has to be performed from the metastable triplet states with lifetimes of only a few tens of milliseconds, a fast measurement technique all the way from the production to the probing of the ion is necessary. This limits the usage of ion-trap techniques for this application, but we have demonstrated that collinear laser spectroscopy can reach comparable precision. Supported by high-precision atomic structure calculations [72–74], measurements with He-like boron at our level of accuracy will be sufficient to decrease the uncertainty of the absolute mean-square nuclear charge radii of ^{10,11}B by more than two orders of magnitude compared with results from elastic electron-scattering experiments [13,14]. Subsequent measurement campaigns with stable isotopes of other light He-like systems such as Li$^+$, Be^{2+}, C^{4+}, and N^{5+} are needed and would substantially benefit from our results.

[1] P. Campbell, I. D. Moore, and M. R. Pearson, Laser spectroscopy for nuclear structure physics, Prog. Part. Nucl. Phys. **86**, 127 (2016).

[2] M. T. Murphy and J. C. Berengut, Laboratory atomic transition data for precise optical quasar absorption spectroscopy, Mon. Not. R. Astron. Soc. **438**, 388 (2013).

[3] V. V. Flambaum and S. G. Porsev, Enhanced sensitivity to the fine-structure-constant variation in the Th IV atomic clock transition, Phys. Rev. A **80**, 064502 (2009).

[4] Z.-T. Lu and K. D. A. Wendt, Laser-based methods for ultrasensitive trace-isotope analyses, Rev. Sci. Instrum. **74**, 1169 (2003).

[5] J. C. Berengut, V. A. Dzuba, V. V. Flambaum, J. A. King, M. G. Kozlov, M. T. Murphy, and J. K. Webb, Atomic transition frequencies, isotope shifts, and sensitivity to variation of the fine structure constant for studies of quasar absorption spectra, in *From Varying Couplings to Fundamental Physics*, edited by C. Martins and P. Molaro (Springer, Berlin, 2011), pp. 9–16.

[6] C. Frugiuele, E. Fuchs, G. Perez, and M. Schlaffer, Constraining new physics models with isotope shift spectroscopy, Phys. Rev. D **96**, 015011 (2017).

[7] J. C. Berengut, D. Budker, C. Delaunay, V. V. Flambaum, C. Frugiuele, E. Fuchs, C. Grojean, R. Harnik, R. Ozeri, G. Perez, and Y. Soreq, Probing New Long-Range Interactions by Isotope Shift Spectroscopy, Phys. Rev. Lett. **120**, 091801 (2018).

[8] V. V. Flambaum, A. J. Geddes, and A. V. Viatkina, Isotope shift, nonlinearity of King plots, and the search for new particles, Phys. Rev. A **97**, 032510 (2018).

[9] I. Counts, J. Hur, D. P. L. Aude Craik, H. Jeon, C. Leung, J. C. Berengut, A. Geddes, A. Kawasaki, W. Jhe, and V. Vuletić, Evidence for Nonlinear Isotope Shift in Yb$^+$ Search for New Boson, Phys. Rev. Lett. **125**, 123002 (2020).

[10] P.-G. Reinhard, W. Nazarewicz, and R. F. Garcia Ruiz, Beyond the charge radius: The information content of the fourth radial moment, Phys. Rev. C **101**, 021301(R) (2020).

[11] C. Shi, F. Gebert, C. Gorges, S. Kaufmann, W. Nörtershäuser, B. K. Sahoo, A. Surzhykov, V. A. Yerokhin, J. C. Berengut, F. Wolf, J. C. Heip, and P. O. Schmidt, Unexpectedly large difference of the electron density at the nucleus in the $4p\ ^2P_{1/2,3/2}$ fine-structure doublet of Ca$^+$, Appl. Phys. B: Lasers Opt. **123**, 2 (2017).

[12] B. Maaß, T. Hüther, K. König, J. Krämer, J. Krause, A. Lovato, P. Müller, K. Pachucki, M. Puchalski, R. Roth, R. Sánchez, F. Sommer, R. B. Wiringa, and W. Nörtershäuser, Nuclear Charge Radii of ^{10,11}B, Phys. Rev. Lett. **122**, 182501 (2019).

[13] T. Stovall, J. Goldemberg, and D. Isabelle, Coulomb form factors of ^{10}B and ^{11}B, Nucl. Phys. **86**, 225 (1966).

[14] A. Cichocki, J. Dubach, R. S. Hicks, G. A. Peterson, C. W. de Jager, H. de Vries, N. Kalantar-Nayestanaki, and T. Sato, Electron scattering from ^{10}B, Phys. Rev. C **51**, 2406 (1995).

[15] R. F. Garcia Ruiz, M. L. Bissell, K. Blaum, A. Ekström, N. Frömmgen, G. Hagen, M. Hammen, K. Hebeler, J. D. Holt, G. R. Jansen, M. Kowalska, K. Kreim, W. Nazarewicz, R. Neugart, G. Neyens, W. Nörtershäuser, T. Papenbrock, J. Papuga, A. Schwenk, J. Simonis *et al.*, Unexpectedly large charge radii of neutron-rich calcium isotopes, Nat. Phys. **12**, 594 (2016).

[16] A. J. Miller, K. Minamisono, A. Klose, D. Garand, C. Kujawa, J. D. Lantis, Y. Liu, B. Maaß, P. F. Mantica, W. Nazarewicz, W. Nörtershäuser, S. V. Pineda, P.-G. Reinhard, D. M. Rossi, F. Sommer, C. Sumithrarachchi, A. Teigelhöfer, and J. Watkins, Proton superfluidity and charge radii in proton-rich calcium isotopes, Nat. Phys. **15**, 432 (2019).

[17] H. J. Emrich, G. Fricke, G. Mallot, H. Miska, H.-G. Sieberling, J. M. Cavedon, B. Frois, and D. Goutte, Radial distribution of nucleons in the isotopes ^{48,40}Ca, Nucl. Phys. A **396**, 401 (1983).

[18] H. D. Wohlfahrt, E. B. Shera, M. V. Hoehn, Y. Yamazaki, and R. M. Steffen, Nuclear charge distributions in $1f_{\frac{7}{2}}$-shell nuclei from muonic x-ray measurements, Phys. Rev. C **23**, 533 (1981).

[19] C. W. P. Palmer, P. E. G. Baird, S. A. Blundell, J. R. Brandenberger, C. J. Foot, D. N. Stacey, and G. K. Woodgate, Laser spectroscopy of calcium isotopes, J. Phys. B: At. Mol. Phys. **17**, 2197 (1984).

[20] B. Cheal, T. E. Cocolios, and S. Fritzsche, Laser spectroscopy of radioactive isotopes: Role and limitations of

accurate isotope-shift calculations, Phys. Rev. A **86**, 042501 (2012).

[21] Z.-C. Yan and G. W. F. Drake, Lithium isotope shifts as a measure of nuclear size, Phys. Rev. A **61**, 022504 (2000).

[22] M. Puchalski and K. Pachucki, Relativistic, QED, and finite nuclear mass corrections for low-lying states of Li and Be$^+$, Phys. Rev. A **78**, 052511 (2008).

[23] Z.-C. Yan, W. Nörtershäuser, and G. W. F. Drake, High Precision Atomic Theory for Li and Be$^+$: QED Shifts and Isotope Shifts, Phys. Rev. Lett. **100**, 243002 (2008).

[24] M. L. Bissell, T. Carette, K. T. Flanagan, P. Vingerhoets, J. Billowes, K. Blaum, B. Cheal, S. Fritzsche, M. Godefroid, M. Kowalska, J. Krämer, R. Neugart, G. Neyens, W. Nörtershäuser, and D. T. Yordanov, Cu charge radii reveal a weak sub-shell effect at $N = 40$, Phys. Rev. C **93**, 064318 (2016).

[25] B. K. Sahoo, A. R. Vernon, R. F. G. Ruiz, C. L. Binnersley, J. Billowes, M. L. Bissell, T. E. Cocolios, G. J. Farooq-Smith, K. T. Flanagan, W. Gins, R. P. de Groote, A. Koszorus, G. Neyens, K. M. Lynch, F. Parnefjord-Gustafsson, C. M. Ricketts, K. D. A. Wendt, S. G. Wilkins, and X. F. Yang, Analytic response relativistic coupled-cluster theory: The first application to indium isotope shifts, New J. Phys. **22**, 012001 (2020).

[26] S. Raeder, D. Ackermann, H. Backe, R. Beerwerth, J. C. Berengut, M. Block, A. Borschevsky, B. Cheal, P. Chhetri, C. E. Düllmann, V. A. Dzuba, E. Eliav, J. Even, R. Ferrer, V. V. Flambaum, S. Fritzsche, F. Giacoppo, S. Götz, F. P. Heßberger, M. Huyse *et al.*, Probing Sizes and Shapes of Nobelium Isotopes by Laser Spectroscopy, Phys. Rev. Lett. **120**, 232503 (2018).

[27] Y. Wan, F. Gebert, J. B. Wübbena, N. Scharnhorst, S. Amairi, I. D. Leroux, B. Hemmerling, N. Lörch, K. Hammerer, and P. O. Schmidt, Precision spectroscopy by photon-recoil signal amplification, Nat. Commun. **5**, 3096 (2014).

[28] F. Gebert, Y. Wan, F. Wolf, C. N. Angstmann, J. C. Berengut, and P. O. Schmidt, Precision Isotope Shift Measurements in Calcium Ions Using Quantum Logic Detection Schemes, Phys. Rev. Lett. **115**, 053003 (2015).

[29] P. Kumar, C.-B. Li, and B. K. Sahoo, Diverse trends of electron correlation effects for properties with different radial and angular factors in an atomic system: A case study in Ca$^+$, J. Phys. B: At., Mol. Opt. Phys. **51**, 055101 (2018).

[30] K. Wendt, S. A. Ahmad, F. Buchinger, A. C. Mueller, R. Neugart, and E. W. Otten, Relativistic J-dependence of the isotope shift in the 6s-6p doublet of Ba II, Z. Phys. A: At. Nucl. **318**, 125 (1984).

[31] P. Imgram, K. König, J. Krämer, T. Ratajczyk, R. A. Müller, A. Surzhykov, and W. Nörtershäuser, Collinear laser spectroscopy at ion-trap accuracy: Transition frequencies and isotope shifts in the $6s\ ^2S_{1/2} \rightarrow 6p\ ^2P_{1/2,3/2}$ transitions in Ba$^+$, Phys. Rev. A **99**, 012511 (2019).

[32] C. Gorges, K. Blaum, N. Frömmgen, C. Geppert, M. Hammen, S. Kaufmann, J. Krämer, A. Krieger, R. Neugart, R. Sánchez, and W. Nörtershäuser, Isotope shift of ^{40,42,44,48}Ca in the $4s\ ^2S_{1/2} \rightarrow 4p\ ^2P_{3/2}$ transition, J. Phys. B: At., Mol. Opt. Phys. **48**, 245008 (2015).

[33] A. Kramida, Isotope shifts in neutral and singly-ionized calcium, At. Data Nucl. Data Tables **133–134**, 101322 (2020).

[34] K. König, J. Krämer, C. Geppert, P. Imgram, B. Maaß, T. Ratajczyk, and W. Nörtershäuser, A new Collinear Apparatus for Laser Spectroscopy and Applied Science (COALA), Rev. Sci. Instrum. **91**, 081301 (2020).

[35] J. Krämer, K. König, C. Geppert, P. Imgram, B. Maaß, J. Meisner, E. W. Otten, S. Passon, T. Ratajczyk, J. Ullmann, and W. Nörtershäuser, High-voltage measurements on the 5 ppm relative uncertainty level with collinear laser spectroscopy, Metrologia **55**, 268 (2018).

[36] W. H. King, Isotope shifts in x-ray spectra, in *Isotope Shifts in Atomic Spectra*, Physics of Atoms and Molecules, edited by P. G. Burke and H. Kleinpoppen (Springer, Boston, 1984), Chap. 5, pp. 55–61.

[37] R. Neugart, Laser spectroscopy on mass-separated radioactive beams, Nucl. Instrum. Methods Phys. Res. **186**, 165 (1981).

[38] A. C. Mueller, F. Buchinger, W. Klempt, E. W. Otten, R. Neugart, C. Ekström, and J. Heinemeier, Spins, moments and charge radii of barium isotopes in the range $^{122-146}$Ba determined by collinear fast-beam laser spectroscopy, Nucl. Phys. A **403**, 234 (1983).

[39] U. Berzinsh, M. Gustafsson, D. Hanstorp, A. Klinkmüller, U. Ljungblad, and A.-M. Mårtensson-Pendrill, Isotope shift in the electron affinity of chlorine, Phys. Rev. A **51**, 231 (1995).

[40] E. W. Otten, Nuclear radii and moments of unstable isotopes, in *Nuclei Far From Stability*, Treatise on Heavy Ion Science Vol. 8, edited by D. A. Bromley (Springer, Boston, 1989), Chap. 7, pp. 517–638.

[41] K. Blaum, J. Dilling, and W. Nörtershäuser, Precision atomic physics techniques for nuclear physics with radioactive beams, Phys. Scr. **2013**, 014017 (2013).

[42] W. H. Wing, G. A. Ruff, W. E. Lamb, and J. J. Spezeski, Observation of the Infrared Spectrum of the Hydrogen Molecular Ion HD$^+$, Phys. Rev. Lett. **36**, 1488 (1976).

[43] E. Riis, H. G. Berry, O. Poulsen, S. A. Lee, and S. Y. Tang, Absolute wavelength measurement and fine-structure determination in ^{7}Li II, Phys. Rev. A **33**, 3023 (1986).

[44] E. Riis, L. U. A. Andersen, N. Bjerre, O. Poulsen, S. A. Lee, and J. L. Hall, Test of the Isotropy of the Speed of Light Using Fast-Beam Laser Spectroscopy, Phys. Rev. Lett. **60**, 81 (1988).

[45] E. Riis, A. G. Sinclair, O. Poulsen, G. W. F. Drake, W. R. C. Rowley, and A. P. Levick, Lamb shifts and hyperfine structure in ^{6}Li$^+$ and ^{7}Li$^+$: Theory and experiment, Phys. Rev. A **49**, 207 (1994).

[46] O. Poulsen, Velocity and high-voltage measurements using resonant collinear, fast-beam/laser interactions, Nucl. Instrum. Methods Phys. Res. **202**, 503 (1982).

[47] O. Poulsen and E. Riis, Absolute determination of high voltages using fast-beam laser velocimetry, Metrologia **25**, 147 (1988).

[48] S. Götte, K.-M. Knaak, N. Kotovski, H.-J. Kluge, G. Ewald, and K. D. A. Wendt, Test of collinear spectroscopy for precise high-voltage determination, Rev. Sci. Instrum. **75**, 1039 (2004).

[49] B. Cheal and K. T. Flanagan, Progress in laser spectroscopy at radioactive ion beam facilities, J. Phys. G: Nucl. Part. Phys. **37**, 113101 (2010).

[50] A. Krieger, C. Geppert, R. Catherall, F. Hochschulz, J. Krämer, R. Neugart, S. Rosendahl, J. Schipper, E. Siesling, C. Weinheimer, D. T. Yordanov, and W. Nörtershäuser, Calibration of the ISOLDE acceleration voltage using a high-precision voltage divider and applying collinear fast beam laser spectroscopy, Nucl. Instrum. Methods Phys. Res., Sect. A **632**, 23 (2011).

[51] S. Bauer, R. Berendes, F. Hochschulz, H.-W. Ortjohann, S. Rosendahl, T. Thümmler, M. Schmidt, and C. Weinheimer,

Next generation KATRIN high precision voltage divider for voltages up to 65 kV, J. Instrum. **8**, P10026 (2013).

[52] B. Maaß, K. König, J. Krämer, A. J. Miller, K. Minamisono, W. Nörtershäuser, and F. Sommer, A 4π fluorescence detection region for collinear laser spectroscopy, arXiv:2007.02658.

[53] M. Hettrich, T. Ruster, H. Kaufmann, C. F. Roos, C. T. Schmiegelow, F. Schmidt-Kaler, and U. G. Poschinger, Measurement of Dipole Matrix Elements with a Single Trapped Ion, Phys. Rev. Lett. **115**, 143003 (2015).

[54] Z. Meir, M. Sinhal, M. S. Safronova, and S. Willitsch, Combining experiments and relativistic theory for establishing accurate radiative quantities in atoms: The lifetime of the $^2P_{3/2}$ state in ^{40}Ca$^+$, Phys. Rev. A **101**, 012509 (2020).

[55] M. Kretzschmar, S. Götte, G. Ewald, K.-M. Knaak, K. D. A. Wendt, and H.-J. Kluge, Influence of the thermal motion on the line shape and position of resonances in collinear fast beam laser spectroscopy, Appl. Phys. B: Lasers Opt. **79**, 623 (2004).

[56] C. J. Sansonetti, C. E. Simien, J. D. Gillaspy, J. N. Tan, S. M. Brewer, R. C. Brown, S. Wu, and J. V. Porto, Absolute Transition Frequencies and Quantum Interference in a Frequency Comb Based Measurement of the ^{6,7}Li D Lines, Phys. Rev. Lett. **107**, 023001 (2011).

[57] R. C. Brown, S. Wu, J. V. Porto, C. J. Sansonetti, C. E. Simien, S. M. Brewer, J. N. Tan, and J. D. Gillaspy, Quantum interference and light polarization effects in unresolvable atomic lines: Application to a precise measurement of the ^{6,7}Li D_2 lines, Phys. Rev. A **87**, 032504 (2013).

[58] A. Beyer, L. Maisenbacher, A. Matveev, R. Pohl, K. Khabarova, A. Grinin, T. Lamour, D. C. Yost, T. W. Hänsch, N. Kolachevsky, and T. Udem, The Rydberg constant and proton size from atomic hydrogen, Science **358**, 79 (2017).

[59] A.-M. Mårtensson-Pendrill, A. Ynnerman, H. Warston, L. Vermeeren, R. E. Silverans, A. Klein, R. Neugart, C. Schulz, P. Lievens, and The ISOLDE Collaboration, Isotope shifts and nuclear-charge radii in singly ionized $^{40-48}$Ca, Phys. Rev. A **45**, 4675 (1992).

[60] W. Nörtershäuser, K. Blaum, K. Icker, P. Müller, A. Schmitt, K. Wendt, and B. Wiche, Isotope shifts and hyperfine constants in the 3d ^{2}D$_J$ →4p ^{2}P$_J$ transitions in calcium II, Eur. Phys. J. D **2**, 33 (1998).

[61] M. Chwalla, J. Benhelm, K. Kim, G. Kirchmair, T. Monz, M. Riebe, P. Schindler, A. S. Villar, W. Hänsel, C. F. Roos, R. Blatt, M. Abgrall, G. Santarelli, G. D. Rovera, and P. Laurent, Absolute Frequency Measurement of the ^{40}Ca$^+$ $4s\ ^2S_{1/2} - 3d\ ^2D_{5/2}$ Clock Transition, Phys. Rev. Lett. **102**, 023002 (2009).

[62] H. Guan, Y. Huang, P.-L. Liu, W. Bian, H. Shao, and K.-L. Gao, Precision spectroscopy with a single ^{40}Ca$^+$ ion in a Paul trap, Chin. Phys. B **24**, 054213 (2015).

[63] C. Solaro, S. Meyer, K. Fisher, M. V. DePalatis, and M. Drewsen, Direct Frequency-Comb-Driven Raman Transitions in the Terahertz Range, Phys. Rev. Lett. **120**, 253601 (2018).

[64] F. W. Knollmann, A. N. Patel, and S. C. Doret, Part-per-billion measurement of the $4\ ^2S_{1/2} \rightarrow 3\ ^2D_{5/2}$ electric-quadrupole-transition isotope shifts between ^{42,44,48}Ca$^+$ and ^{40}Ca$^+$, Phys. Rev. A **100**, 022514 (2019).

[65] C. Solaro, S. Meyer, K. Fisher, J. C. Berengut, E. Fuchs, and M. Drewsen, Improved Isotope-Shift-Based Bounds on Bosons beyond the Standard Model through Measurements of the $^2D_{3/2} - ^2D_{5/2}$ Interval in Ca$^+$, Phys. Rev. Lett. **125**, 123003 (2020).

[66] M. Wang, G. Audi, F. G. Kondev, W. Huang, S. Naimi, and X. Xu, The AME2016 atomic mass evaluation (II). Tables, graphs and references, Chin. Phys. C **41**, 030003 (2017).

[67] D. York, N. M. Evensen, M. L. Martínez, and J. De Basabe Delgado, Unified equations for the slope, intercept, and standard errors of the best straight line, Am. J. Phys. **72**, 367 (2004).

[68] M. S. Safronova and W. R. Johnson, Third-order isotope-shift constants for alkali-metal atoms and ions, Phys. Rev. A **64**, 052501 (2001).

[69] G. Fricke and K. Heilig, Nuclear Charge Radii, *Landolt-Börnstein: Numerical Data and Functional Relationships in Science and Technology: New Series Vol. 20*, edited by H. Schopper (Springer, Berlin, 2004), pp. 54–59.

[70] M. Hammen, W. Nörtershäuser, D. L. Balabanski, M. L. Bissell, K. Blaum, I. Budinčević, B. Cheal, K. T. Flanagan, N. Frömmgen, G. Georgiev, C. Geppert, M. Kowalska, K. Kreim, A. Krieger, W. Nazarewicz, R. Neugart, G. Neyens, J. Papuga, P.-G. Reinhard, M. M. Rajabali *et al.*, From Calcium to Cadmium: Testing the Pairing Functional Through Charge Radii Measurements of $^{100-130}$Cd, Phys. Rev. Lett. **121**, 102501 (2018).

[71] P. Micke, T. Leopold, S. A. King, E. Benkler, L. J. Spieß, L. Schmöger, M. Schwarz, J. R. Crespo López-Urrutia, and P. O. Schmidt, Coherent laser spectroscopy of highly charged ions using quantum logic, Nature (London) **578**, 60 (2020).

[72] V. A. Yerokhin, V. Patkóš, and K. Pachucki, Relativistic corrections to the Bethe logarithm for the $2\ ^3S$ and $2\ ^3P$ states of He, Phys. Rev. A **98**, 032503 (2018).

[73] V. Patkóš, V. A. Yerokhin, and K. Pachucki, Complete quantum electrodynamic α^6m correction to energy levels of light atoms, Phys. Rev. A **100**, 042510 (2019).

[74] V. Patkóš, V. A. Yerokhin, and K. Pachucki, Nonradiative α^7m QED effects in Lamb shift of helium triplet states, Phys. Rev. A **101**, 062516 (2020).